An experimental study of the thermal-hydraulics of a spent nuclear fuel pool under loss-of-cooling accident conditions Part II: a first interpretation of the MIDI tests

Jimmy Martin, Benoît Migot

An experimental study of the thermal-hydraulics of a spent nuclear fuel pool under loss-of-cooling accident conditions

Part II: a first interpretation of the MIDI tests

J. Martin* and B. Migot

Institut de Radioprotection et de Sûreté Nucléaire, PSN-RES, CEN Cadarache, BP3, 13115, Saint-Paul-lez-Durance, France

*corresponding author: jimmy.martin@irsn.fr

Abstract

This article provides a first interpretation of the MIDI tests that were conducted in the frame of the IRSN's DENOPI project. A first-level phenomenological analysis is detailed here. It is shown that the actual phenomenology mostly complies with the one that was envisioned by the community right after the Fukushima-Daiichi nuclear accident. Next, the diverse modes of water vaporization that may come into play during a spent nuclear fuel pool loss-of-cooling accident are quantified for each achieved test, by means of a proposed analytical model of the vapor diffusion process taking place on top of the liquid pool free surface. Then, a so-called vaporization regimes map is reconstructed on the basis of the test data. This map allows predicting the most likely dominant vaporization mode, given the pool level and total heat power. At last, the obtained data is reduced through the form of a set of dimensionless correlations, involving some of the classical numbers in heat and mass transfers. In doing so, the free surface evaporation, degassing of dissolved gaseous species and bubbles release processes are all modeled by means of a simple mathematical formulation.

Keywords

Gravity-driven flashing, superheated water, free surface evaporation, pool boiling, integral scale experiment.

1. INTRODUCTION

Following the March 11, 2011 Fukushima-Daiichi nuclear power plant accident which brought to light the vulnerability of spent-fuel-pools (SFP), a wealth of phenomenological analyses has been conducted worldwide regarding the thermal-hydraulic aspects of SFP loss-of-cooling transients. Significantly, the *Electric Power Research Institute* published in 2012 a first in-depth analysis of the behavior of the Fukushima-Daiichi nuclear power plant SFPs throughout the March 11, 2011 accident [1]. Later on, two international working groups investigated this very topic under the auspices of the *Nuclear Energy Agency* of the *Organisation for Economic Cooperation and Development* and shared their conclusions with the community by means of two public reports, respectively published in 2014 [2] and 2018 [3]. Overall, all those analytical activities proposed a first image of what a SFP loss-of-cooling accident could be, before the fuels get uncovered. Let us first depict what was envisioned at the time.

According to the community, when a SFP loss-of-cooling accident initiates, a natural convection flow is expected to develop between the hot spent fuels, stored vertically at the bottom of the pool, and the colder water free surface and concrete walls of the basin, as illustrated in Figure 1. The heat convected that way is then supposed to be lost by a combination of wall heat conduction and water vaporization [1]. Whatever the liquid bulk temperature, the continuous heat supply toward the free surface may lead to water evaporation, the ubiquitous and first vaporization mode that is expected to occur in such configuration. It is to be noted that this vaporization mode does not involve any bubble nucleation process. Two other modes may also contribute to water vaporization in the course of this accident: the nucleate boiling of water along the spent fuels and the gravity-driven flashing of superheated water [3]. Those modes are based on bubble nucleation, a phase change process which is triggered by the presence of pre-existing gas *nuclei* (*i.e.* tiny bubbles) within the liquid or onto immersed solid surfaces and the reach of local liquid superheats and/or dissolved gases supersaturation [4]. The nucleate boiling specifically refers to the bubble nucleation that may occur onto the hot rods of the stored spent fuels. It depends on the overall flow pattern associated with the natural convection heat transfer developing at pool scale. The gravity-driven flashing of superheated water is in turn a singular phenomenon which is usually met in *geysers* [5]. It is more generally found in any sufficiently large vertical system, where an uprising heated fluid experiences a significant decrease in hydrostatic pressure and associated saturation temperature [6]. Under those conditions, the liquid may reach a so-called superheated, metastable state and may spontaneously turn into bubbles to recover a state of stable thermodynamic equilibrium, a process named *flashing* [7]. The spontaneous bubbly flashing is however only achieved when numerous gaseous *nuclei* are present within the liquid [8]. Precisely, another phenomenon may lead to a significant production of those *nuclei* within the water bulk: the degassing of the initially present dissolved non-condensable species such as the atmospheric oxygen and nitrogen [9]. Those gases are indeed prompt to escape from the water bulk, through the form of bubbles, when their solubility drops. The latter process may be for instance the consequence of the water heat up. At last, the heat losses through the walls are typically much smaller than the stored decay heat, which can be as large as a dozen megawatt [1]. Hence in most of the studied *scenarii*, the water gradually heats up till an energetic equilibrium is reached with the heat removal achieved by the above vaporization modes.

At that time, many questions were formulated on the basis of this postulated phenomenological image. First of all, the gravity-driven flashing was judged hypothetical in the specific configuration of a pool and the existence of any possible liquid superheat still debated, as reflected in [3] (*cf.* the low level-of-

knowledge and experts' vote scattering, associated with the phenomenon). One unclear point was related to the existence of enough gaseous *nuclei* within the liquid bulk to promote flashing at that very location. Indeed, the kinetics associated with the degassing process of the non-condensable dissolved species was yet uncertain and as mentioned above, this physical mechanism may yield a significant amount of freely-floating *gas nuclei*. For that reason, it was first assumed that, if existing, the flashing would take place preferentially onto any immersed solid and rough surface, as suggested for instance in [8]. Next, the final system's energetic equilibrium was to be better understood. In particular, there was an interest in defining which vaporization mode would mainly explain the overall water vaporization process under some given set of initial and boundary conditions. Indeed, it was early recognized that if bubbles were to nucleate in the course of an accident, this would in turn prevent any restarting of the SFP cooling system and would contribute to the release of various radionuclides that can be classically met within the SFP water, well before the spent nuclear fuels get uncovered [3]. Among the conditions that were assumed as playing a role on the above vaporization modes is the type of loading pattern of the stored spent fuels, whose effect on the SFP energy budget needed to be investigated. At last, it was consensually admitted in 2018 that the prediction of the natural convection flow that is expected to develop at pool scale was an issue in the general case of a heterogeneous spent fuels loading within the SFP [3]. The issue, judged as important with regards to the SFP safety [10], included the understanding of the two-phase instabilities that may potentially arise from a heterogeneous spent fuels loading, when no crossflows are practically possible within the storage racks [11].

In order to address those issues, the French *Institut de Radioprotection et de Sûreté Nucléaire* (IRSN) has launched in 2014 a research program, including various experimental and modeling activities. As part of this program, the so-called DENOPI project was initiated this same year and ended in 2022 [12]. Especially, the scientific objectives of the DENOPI project led to the definition and construction of the so-called MIDI facility, topic of the present paper [13]. This one-of-a-kind facility [14] was built as the empirical investigation tool of the first axis of DENOPI, which was dedicated to the study of natural convection and vaporization regimes at the integral scale of a SFP during the studied accident scenario. The MIDI facility and the experimental results obtained to date by means of the latter are largely described in [15]. In turn, the present article proposes a first physical interpretation of the obtained results. After a brief recall of the main features of the MIDI facility (Section 2), the overall image of a SFP loss-of-cooling accident before the fuels uncover, as early envisioned by the community, is compared with the actual phenomenological observations made from the MIDI tests (Section 3). Then, on the basis of an analytical modeling of vapor transport from the SFP free surface, introduced in Section 4.1, the three modes of water vaporization that may come into play throughout the studied accident are quantified for each achieved test, in Section 4.2. An emphasis is made in this very section on the potential effect of the thermal power, loading pattern and initial pool level on the vaporization modes. A so-called *vaporization regimes map* is further reconstructed on the basis of the test data (Section 4.3). At last, the obtained data is reduced through the form of a set of dimensionless correlations, describing both the single and two-phase heat and mass transfers that may develop accidentally in a SFP (Section 5).

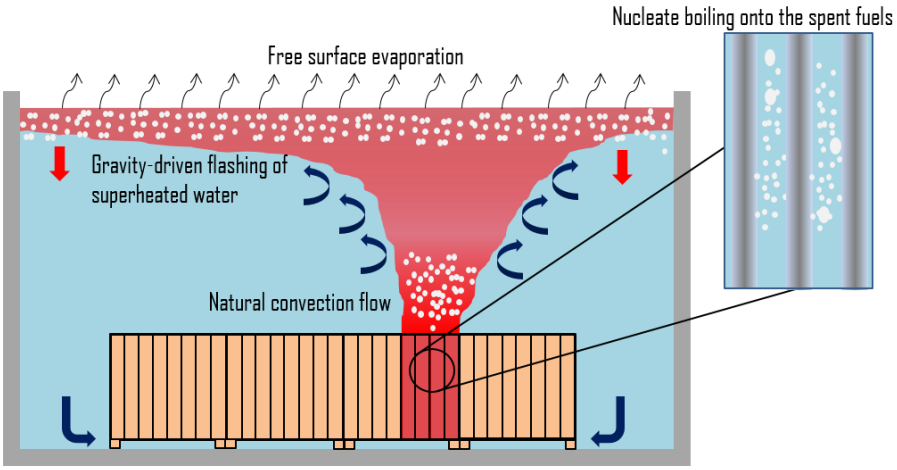

Figure 1: Illustration of the three envisioned water vaporization modes during a SFP loss-of-cooling accident: the free surface evaporation, the nucleate boiling onto the spent fuels and the gravity driven flashing of superheated water.

2. THE MIDI FACILITY AND ITS TEST MATRIX

In this section are provided a recap of the main features characterizing the MIDI facility and a brief description of the tests achieved to date. The interested reader may note, however, that many more details regarding MIDI and the achieved experiments can be found out in [15].

2.1. MIDI features and instrumentation

The MIDI facility, illustrated in Figure 2, is a small scale integral mockup of a typical French Pressurized Water Reactor SFP, whose characteristics are given in Table 1. The heat source, simulating some stored spent nuclear fuels, consists in 21 individual heating elements, each made of 3x3 electrically-heated rods. The heaters are setup through the form of a regular arrangement of 7x3 bundles in a single rack. As usually met in French SFP racks designs, no crossflows are allowed between the bundles, that may be seen as independent hydraulic channels. Moreover, the heaters can be powered individually, thereby allowing the study of the influence of the spent fuels loading pattern on their coolability. The upper part of the pool is a free gaseous volume. MIDI is equipped with a specific metrology to measure local flow characteristics. In details, the measurement of the water pool level is achieved by means of both pressure gauges and a guided-wave radar level probe. Local temperatures are measured within the liquid pool using 9 multipoint sensors, having each 7 Pt-100 class-A probes. The free surface temperature is recorded with a net of infrared sensors. In addition, the use of an electric conductivity probe and of a dissolved oxygen sensor allows an on-line monitoring of the physico-chemistry of the utilized demineralized water. Next, the gas temperature, total pressure, and relative humidity of the gas volume on top the free surface is measured as well, with a multi-parameter probe. At last, the basin is equipped

with a set of optical windows for a direct observation of the produced bubbles with a 25-frame-per-second camera.

Table 1. Geometrical parameters of the MIDI facility and scaling factors.

Parameters	MIDI facility	Typical PWR SFP	Scale ratio
Basin width (m)	1.35	8.5	1/6
Basin length (m)	2.1	12.6	1/6
Free surface area (m^2)	2.8	107	1/36
Maximum water level (m)	4.0	12.0	1/3
Basin height (m)	5.2	12.0 + margin	1/3
Bundle active length (m)	0.67	~4.0	1/6
Rack height (m)	1.32	~4.0	1/3
Bundle width (m)	0.225	0.225	1/1
Bundle porosity (-)	0.61	0.57	1/1
Number of heated cells (-)	21 (7 x 3 network)	792	1/37
Overall rack flow area (m^2)	~0.65	22.86	1/35
Heat power range (kW)	[30;300]	10 000	-
Max. power per bundle (kW)	50	58	6/7
Volumetric power (kW/m^3)	[2.5;24.7]	7.8	-

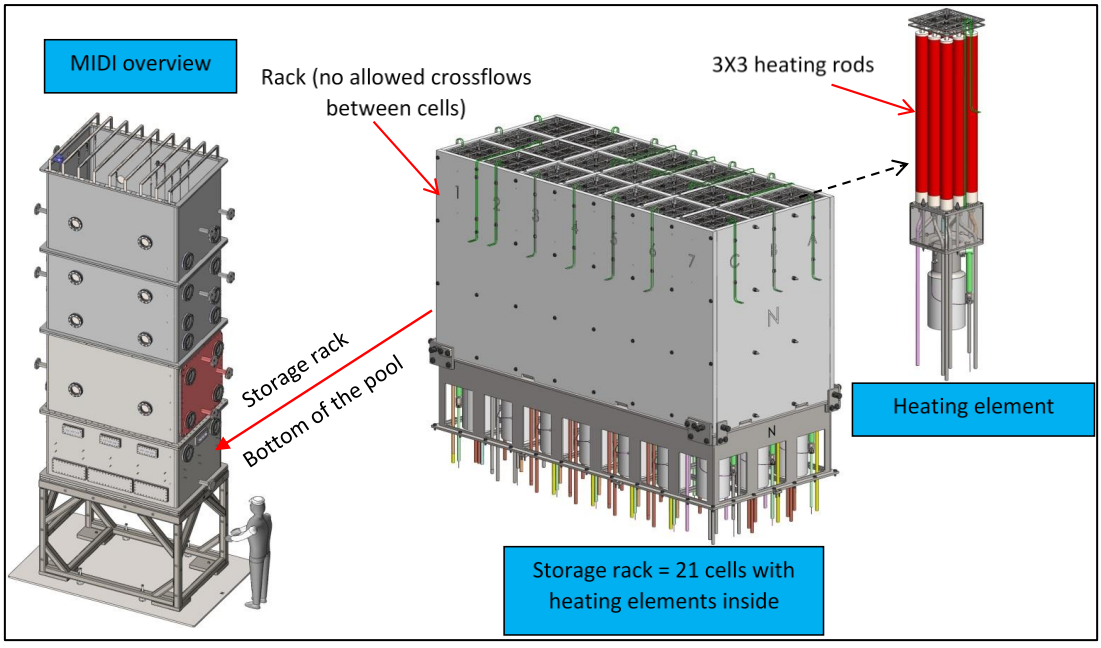

Figure 2: Computer-Aided Design view of MIDI facility and its heated bundles.

2.2. The tests achieved to date

A series of 9 tests, detailed in Table 2, were conducted in the frame of the DENOPI project by varying the following control parameters:

- The total heating power, up to a maximum 300 kW (with a local maximum power of 50 kW per cell);
- The simulated spent fuels loading pattern, as illustrated in Figure 3;
- The initial water level, with two retained values: 4 m or 2 m.

Each test followed a 3-step experimental procedure which is detailed next:

- Stage 1: basin filling, up to the required water level;
- Stage 2: thermal conditioning of the pool at an initial water temperature of 50°C +/- 1.5°C;
- Stage 3: test startup, by imposing a given loading pattern and overall heating power.

At last, those tests were systematically stopped when the remaining water collapsed level reached approximately 50/60 cm above the top of the rack, thereby restricting the presented experiments to the so-called pre-uncovery stage of a SFP loss-of-cooling accident [3].

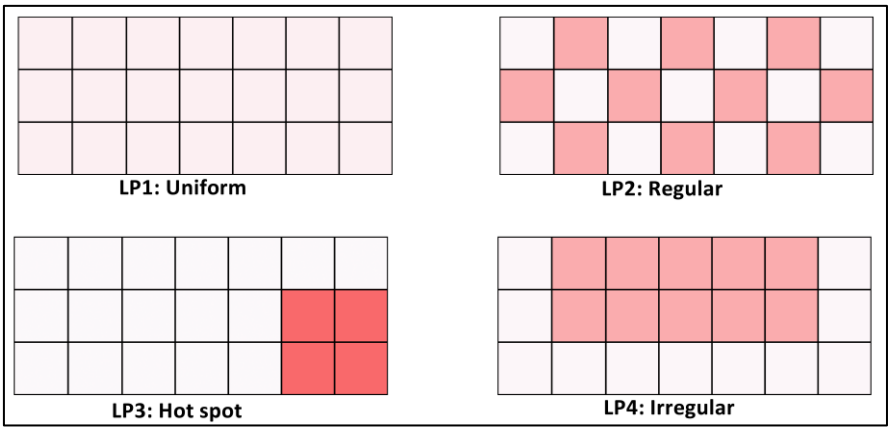

Figure 1: The 4 types of loading pattern tested in MIDI facility.

Table 2. MIDI test matrix.

Test No.	Initial pool level	Loading pattern	Total heat. power	Number of hot cells / Power of hot cells	Number of cold cells / Power of cold cells
1	4 m	LP1	93 kW	21 / 4.4 kW	0 / 0 kW
2	4 m	LP2	93 kW	10 / 8.5 kW	11 / 0.8 kW
3	4 m	LP3	93 kW	4 / 21.2 kW	17 / 0.5 kW
4	4 m	LP4	93 kW	10 / 8.5 kW	11 / 0.8 kW
5	4 m	LP2	300 kW	10 / 27.3 kW	11 / 2.5 kW
6	4 m	LP3	300 kW	4 / 49.5 kW	17 / 6.0 kW
7	2 m	LP2	300 kW	10 / 27.3 kW	11 / 2.5 kW
8	4 m	LP3	220 kW	4 / 50.0 kW	17 / 1.2 kW
9	4 m	LP3	55 kW	4 / 11.4 kW	17 / 0.6 kW

3. A FIRST PHENOMENOLOGICAL ANALYSIS

In what follows is proposed a first answer to the questions, discussed in the introduction of the present paper, that were formulated by the community regarding the thermal-hydraulics of SFP loss-of-cooling accidents. This answer is based on a series phenomenological observations made during the MIDI experiments, presented in [15]. Those observations are occasionally compared with the one achieved at a smaller scale within the IRSN's Aquarius test device, described in [16], for questioning the validity of the conclusions drawn from the MIDI experiment.

3.1. The gravity-driven flashing is a likely phenomenon in pool-type configurations

One of the main phenomenological results that is worth mentioning from the achieved MIDI tests is the existence of a gravity-driven flashing of superheated water in a pool heated from below. In the left-hand-side of Figure 4 is indeed demonstrated the occurrence of bubble nucleation within the liquid bulk of MIDI facility during one of the tests discussed in [15]. Consistently, this process correlates with the measurement of liquid superheats within the MIDI basin. As one can notice, the first bubbles appear in the middle of the picture, *i.e.* far from the heat source and the lateral walls of the basin. Interestingly, as seen in the right-hand-side of this very figure, the phenomenon has been also observed at a smaller scale (1:25) by means of the IRSN's Aquarius facility [16], [17], which gives more confidence regarding the likelihood of the phenomenon in pool-type geometries. Contrarily to the prior assumption that the phenomenon would preferentially occur onto unheated immersed surfaces such as the lateral walls, the latter actually develops within the liquid bulk and almost no bubbles nucleate onto those walls. Most likely, the thermal state of those walls, colder than the superheated liquid, as shown from the temperature measurements presented in [15], may prevent the flashing occurrence from some entrapped gas cavities.

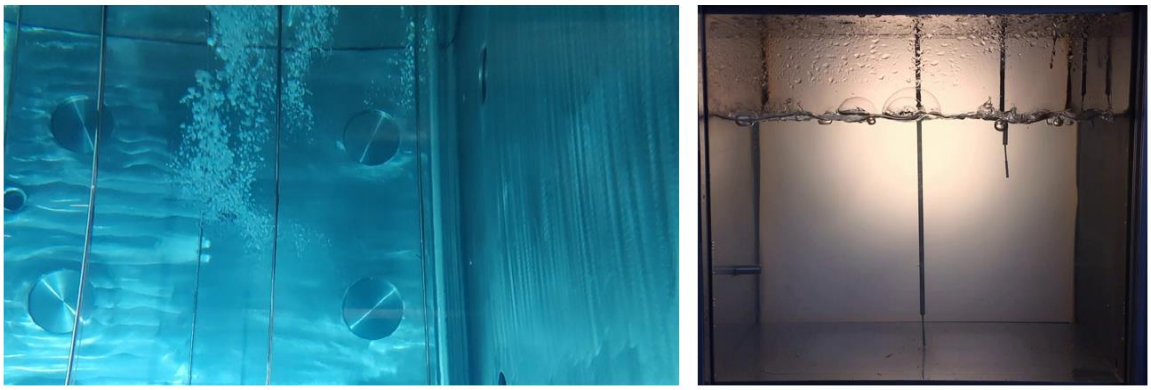

Figure 4: Observation of the gravity-driven pool flashing phenomenon in two test facilities of different scale, operated at IRSN. Left: MIDI test device. Right: Aquarius test device [16], [17].

3.2. The degassing process is mostly completed at MIDI scale when the liquid starts flashing

As mentioned in [15], the degassing of the initially dissolved oxygen was recorded during all achieved tests and the kinetics of the latter process was reported. One can notice from these results that the process

is relatively long and lasts in most of the case till the reach of substantial superheats within the liquid. This means that the dissolved gases are likely to play some role in the occurrence of flashing when the liquid starts superheating, in consistency with what has been observed at a smaller scale, within the Aquarius test device [16], [17]. However during the MIDI tests, the flashing phenomenon typically lasts a long time after the liquid is completely degassed, which questions the origin of the gaseous *nuclei* after the complete depletion in non-condensable species. This point is central to any local modeling of the onset of flashing [18] and hence deserves some finer complementary studies. At this stage, it can be postulated that, even if the degassing process is complete during the long-lasting flashing period, some new *gas nuclei* might be produced by air entrapment from the liquid free surface, when bubbles burst at this very location. In support of this hypothesis, one may note that the above mechanism has been highlighted within the Aquarius test device, as detailed in [16].

3.3. The heat source pattern impacts the void fraction distribution

Next, it is worth mentioning that the type of imposed heat source loading pattern leads to a specific void fraction distribution, when the pool reaches its two-phase regime. Indeed as depicted in Figure 5, the bubbles, be they produced by flashing or boiling, are more likely to nucleate on top of the hottest heated bundles. Pointedly, this result is consistent with another series of observations made by means of the Aquarius test device [16], illustrated in Figure 6. At last, it is to be noted that the MIDI tests presented in [15] yielded no evidence of any two-phase flow instability within the simulated spent fuel bundles.

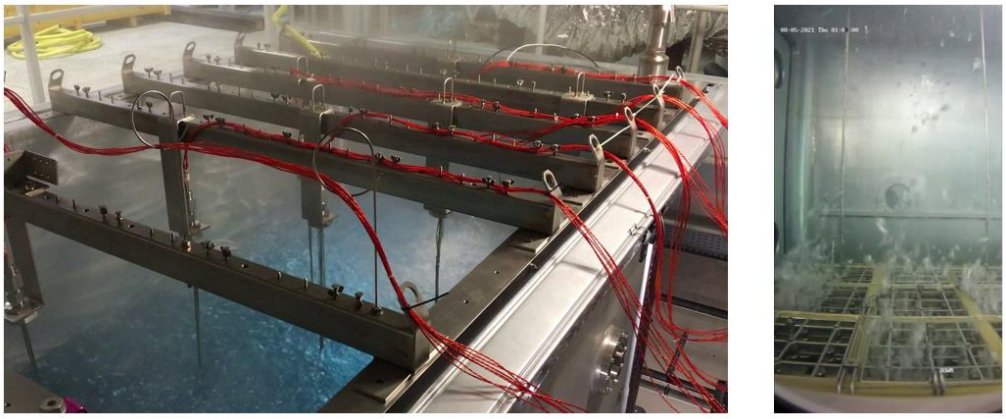

Figure 5: The spatial distribution of the void fraction is tightly linked with the heat source loading pattern. Left: upper view of MIDI's free surface with a bubble plume bursting at its upper corner, *i.e.* right on top of a hot spot loading pattern. Right: bubbles produced only within the hottest heated bundles of MIDI, with a loading pattern corresponding to the type LP2 (*cf.* Figure 3).

(a) Homogeneous heat source (b) Localized heat source

Figure 6: Comparison of two tests performed within the Aquarius device, with a different type of heat source distribution. One can notice that in the case of a localized heating, the flashing occurs only right on top of the heat source [16].

4. A STUDY OF THE VAPORIZATION MODES

In what follows, a focus is made on the diverse vaporization modes that can be observed within MIDI, under some given set of initial and boundary conditions. By means of the MIDI measurements presented in [15] and of an appropriate modeling of the vapor diffusion process occurring on top of the liquid free surface, the magnitude of each vaporization mechanism is later estimated, thereby allowing a better understanding of the pool's energy budget throughout the considered transient.

4.1. Free surface evaporation and bubble mass fluxes

As already discussed, three vaporization modes are expected to come into play during a SFP loss-of-cooling accident [3]. Those modes can be divided into two categories:

- The free surface evaporation;
- The bubble nucleation, which can result from the gravity-driven flashing of superheated water within the liquid bulk and/or from water boiling within the spent fuel bundles.

Let us first denote as j_e and j_b, the two mass fluxes associated with the above two categories, given in kg/m2/s. Then, let us assume the existence of a gas film of thickness δ_g above the free surface, as depicted in Figure 7. This approach, classically referred to as the *film theory* [19], has proven accurate for quantifying the amount of steam produced by free surface evaporation, under similar thermodynamic conditions, by the present authors in [20] and can be hence reasonably applied here.

At the lower-end of this film (*i.e.* at the free surface), the liquid temperature is equal to T_i and is here associated to the performed free surface temperature measurement, detailed in [15]. The vapor molar fraction x_i^v is assumed given by the so-called *Raoult's law*, which reads:

$$x_i^v = \frac{P_{sat}(T_i)}{P_g}$$

with $P_{sat}(T_i)$, the vapor saturation pressure estimated at temperature T_i and P_g, the measured atmospheric pressure on top of the free surface. At this very location, two vapor fluxes are postulated as entering the gas film, namely j_e and j_b. Their sum correspond to j_w, the overall vapor diffusion flux, here estimated from the pool liquid mass measurement, as follows:

$$j_w = j_e + j_b \approx \frac{m_l(t + \Delta t) - m_l(t)}{\Delta t \; S_p}$$

where $m_l(t + \Delta t)$ and $m_l(t)$ are respectively the liquid mass measurement at two distinct times, separated by a time step Δt, and S_p is the liquid free surface area. On top of the film, the boundary temperature is assumed equal to T_g, the gas bulk temperature measurement performed close to the free surface [15]. On the basis of the performed relative humidity measurement ϵ at that very location, one can further estimate the top-end vapor molar fraction x_∞^v as:

$$x_\infty^v = \frac{\epsilon \; P_{sat}(T_g)}{P_g}$$

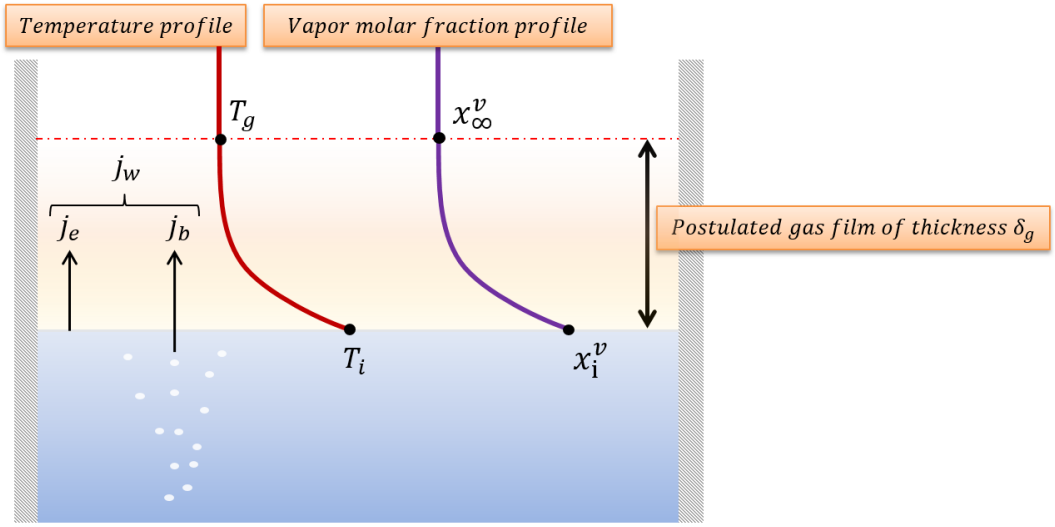

Figure 7: Illustration of the postulated gas film on top of the liquid free surface and its corresponding temperature and vapor molar fraction profiles.

According to the *film theory*, one can show that the overall vapor flux j_w transiting throught the gas film is equal to [21]:

$$j_w = \frac{\overline{\rho_g} \; D_{a-v}}{\delta_g} \text{Log}\left(\frac{x_\infty^v - j_e/j_w}{x_i^v - j_e/j_w}\right)$$

with $\overline{\rho_g}$ and D_{a-v}, respectively the film-averaged gas density and air-vapor diffusion coefficient. The above equation admits two unknown variables in the general case. First is the film thickness δ_g. Under three-dimensional conditions such as in the present study, the latter is often associated with the mass transfer boundary layer that is expected to develop on top of the free surface [19]. This reads:

$$\delta_g = \frac{L_m}{Sh_g}$$

where L_m is some relevant system's characteristic length and Sh_g is the *Sherwood* number characterizing the natural convection mass transfer of vapor that is expected to take place on top of the free surface. In [20], the present authors proposed to use the correlation of *Bower and Saylor*, given in [22], which has proven relevant for reproducing their experimental data. This correlation reads:

$$Sh_g = 0.196\, Sc^{0.5}\, {Ra_m}^{0.322}$$

where Sc and Ra_m are respectively the *Schmidt* and *Rayleigh* mass numbers of the gas bulk, computed as:

$$Sc = \frac{\vartheta_g}{D_{a-v}}$$

$$Ra_m = \frac{g\left(\rho_{g,\infty} - \rho_{g,i}\right) {L_m}^3}{\overline{\rho_g}\,\vartheta_g\,\kappa_g} \approx \frac{g\left(T_i - T_g\right) {L_m}^3}{\overline{T_g}\,\vartheta_g\,\kappa_g}$$

with ϑ_g and κ_g, the gas kinematic viscosity and thermal diffusivity, g, the gravitional acceleration, $\overline{T_g}$ the film-averaged gas temperature, here taken equal to:

$$\overline{T_g} = \frac{1}{2}\left(T_g + T_i\right)$$

In the present study, the characteristic length is taken as the free surface diagonal:

$$L_m = 2.5 \text{ m}$$

The second unknown variable j_e, *i.e.* the evaporation flux generated at the pool free surface, can be solved from the above equation for the overall vapor flux j_w. Once j_e is known and provided j_w, one can then trivially estimate the bubble mass flux j_b exiting the pool through its free surface as:

$$j_b = j_w - j_e$$

This computational method has been applied to the MIDI test results, as presented in the next section, in order to estimate the effect of the overall thermal power, loading pattern and initial pool level on the possible three vaporization modes.

4.2. Thermal power, loading pattern and initial pool level effect on the vaporization modes

Each following figure gathers the results of all tests performed at an equal overall thermal power. In the left-hand-side of those figures is provided the estimate of the free surface evaporation flux j_e. The right-hand-side gives the estimate of the bubble flux j_b. Both fluxes are compared with the overall vapor flux j_w. Bearing in mind the parameters associated with the different tests of the experimental matrix achieved to date (*cf.* Table 2), the cross-comparison of those figures allows studying the effect of the thermal power, loading pattern and initial pool level on the vaporization modes. First of all, one can

observe from all figures that the solved free surface evaporation flux j_e is close to the experimentally known j_w during the single-phase regime of a MIDI test, as expected, which validates the proposed computational method of Section 4.1. Indeed, a lack of vapor bubble nucleation defines this very regime (*i.e.* $j_b = 0$). Consistently, when the liquid temperature reaches its saturation value, j_b starts increasing. At the lowest values of the overall thermal power, a large part of j_w is attributed to the free surface evaporation and j_b is conversely low. This effect tends to reverse as the overall thermal power is increased. As an illustration, during Test #9 performed at a power of roughly 50 kW, the overall vapor flux j_w was almost exclusively attributed to the evaporation till the pool level was low enough for allowing water to boil within the heated bundles (*cf.* Figure 8). This latter condition was fulfilled around 100 hours. Oppositely, during the two-phase regime of Tests #5 and #6, performed at a power of 300 kW, the bubble flux contribution to the overall vaporization flux ranged between 50 and 75% (*cf.* Figure 12). Next, when comparing Tests #5 and #7, performed at an equal thermal power of 300 kW and loading pattern LP2, one can notice that starting a test at a reduced initial pool level leads more rapidly to a higher bubble flux (*cf.* Figures 11 and 12). A low pool level is indeed understood as promoting the water boiling within the heated bundles in an increasing way [23], thereby intensifying the bubble flux j_b. Interestingly, when plotting j_b *versus* the experimentally derived pool collapsed level for Tests #5 and #7, one can observe that the obtained trends are identical (*cf.* Figure 13). Hence, the initial value taken by the pool level does not lead to any so-called *history effect* regarding the magnitude of the bubble mass flux j_b. At last, the study of Figure 9 shows some weak effect of the loading pattern on the time-trend of the bubble mass flux, the patterns LP3 and LP1 yielding respectively the least and the most intense fluxes. Patterns LP2 and LP4 give in turn very similar results. This effect is less visible at a power of 300 kW, as depicted in Figure 12. For now, it is not possible to conclude about the importance of this effect. More tests would indeed be required, by favoring low-power configurations in order to maximize the probability to observe a difference in the produced bubble fluxes.

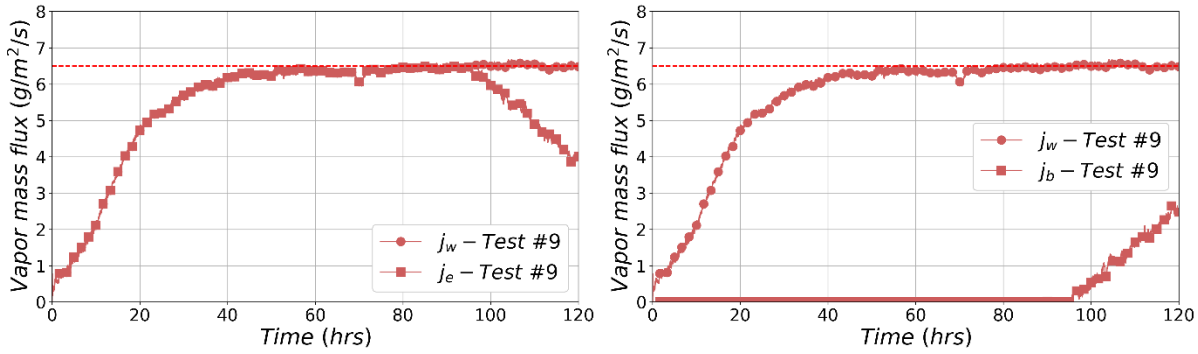

Figure 8: Estimates of the free surface evaporation, bubble and overall mass fluxes j_e, j_b and j_w at a power of 50 kW, loading pattern LP3 and an initial pool level of 4.5 m.

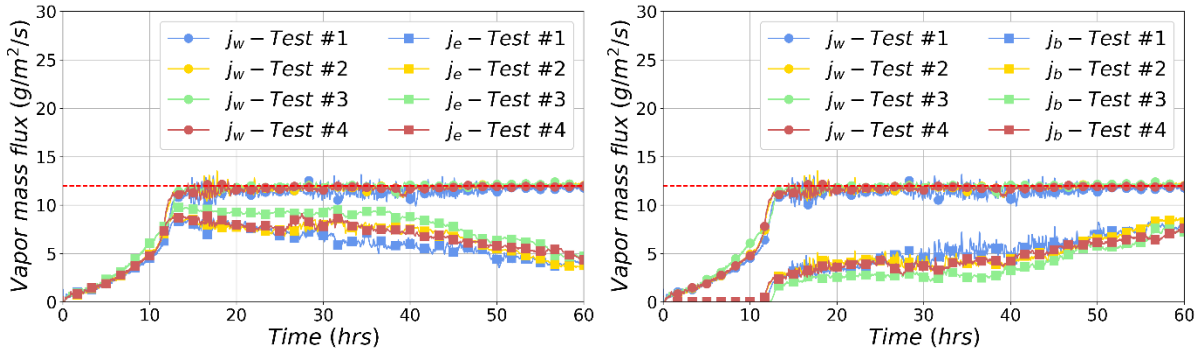

Figure 9: Estimates of the free surface evaporation, bubble and overall mass fluxes j_e, j_b and j_w at a power of 93 kW, loading patterns LP1 to LP4 and an initial pool level of 4.5 m.

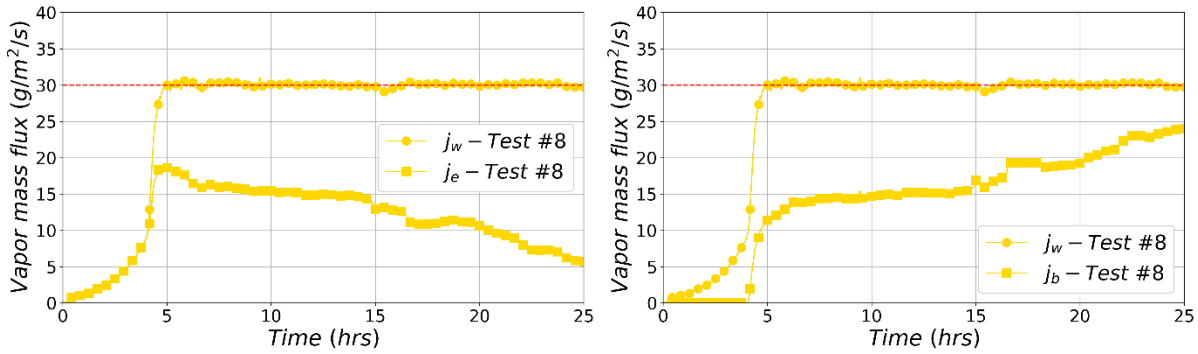

Figure 10: Estimates of the free surface evaporation, bubble and overall mass fluxes j_e, j_b and j_w at a power of 220 kW, loading pattern LP3 and an initial pool level of 4.5 m.

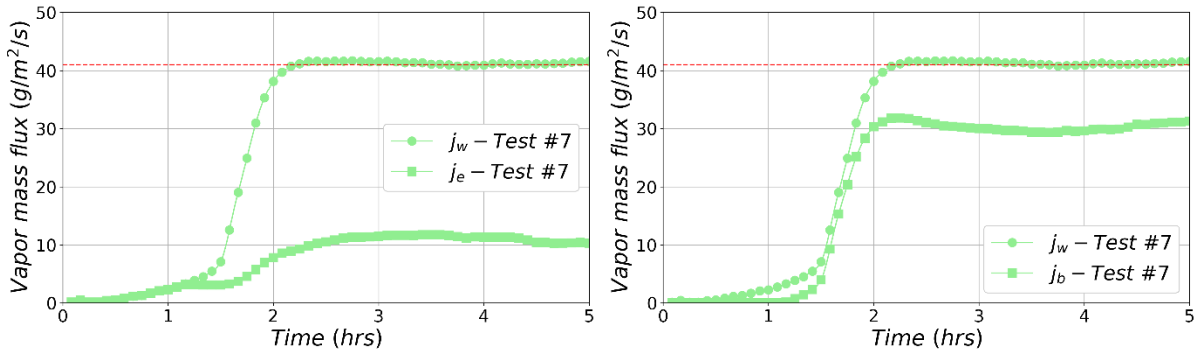

Figure 11: Estimates of the free surface evaporation, bubble and overall mass fluxes j_e, j_b and j_w at a power of 300 kW, loading pattern LP2 and an initial pool level of 2.5 m.

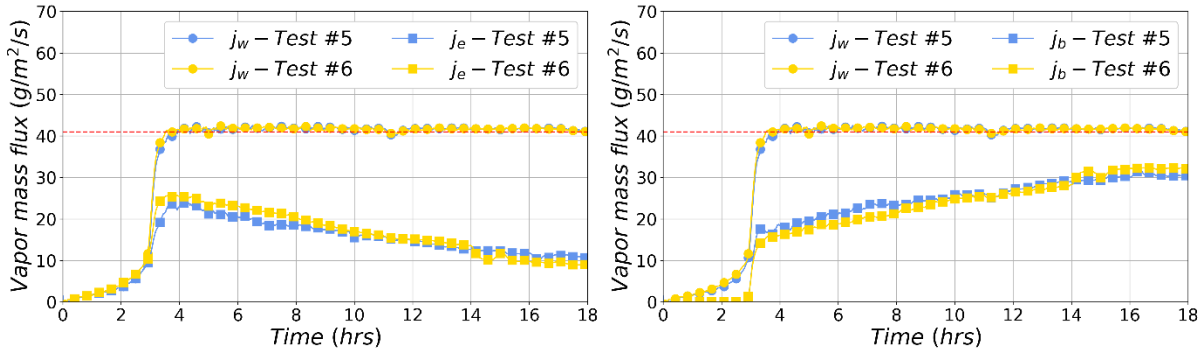

Figure 12: Estimates of the free surface evaporation, bubble and overall mass fluxes j_e, j_b and j_w at a power of 300 kW, loading patterns LP2 and LP3 and an initial pool level of 4.5 m.

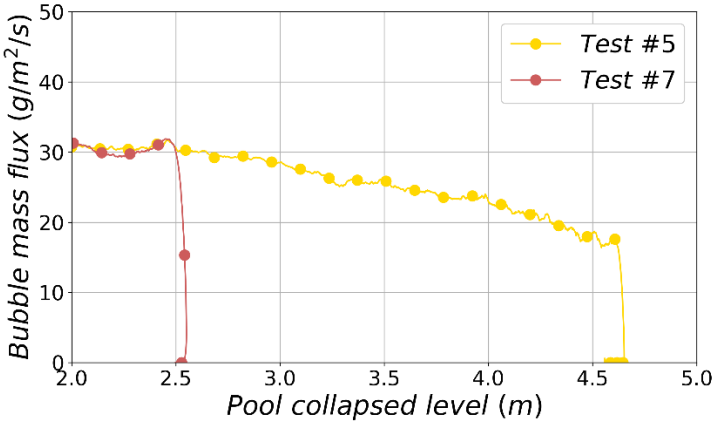

Figure 13: Bubble mass flux *versus* pool collapsed level for Tests #5 and #7, performed at a thermal power of 300 kW, loading pattern LP2 but two different initial pool levels.

4.3. The vaporization regimes map

In the present section, a so-called *vaporization regimes map* is introduced. This map is intended to indicate which vaporization mode dominates the overall liquid pool vaporization, depending on the considered values of the pool collapsed level and total heat power. By choice, for the three domains depicted in the map, the vapor flux corresponding to the indicated vaporization mode exceeds 50% of the overall. Based on a data analysis, the actual MIDI vaporization regimes map was built. For doing so, we first post-processed the bubble mass fluxes given in Figures 8 to 12 and noted the value of the collapsed level from which the computed bubble fluxes exceeded 50% of the overall vaporization flux. The transition collapsed levels estimated that way were then reported into the vaporization regimes map, for each retained heating power. This first stage yielded, by interpolation, the red boundary visible in Figure 14 separating the evaporation mode from the bubbly ones (*i.e.* the flashing and boiling modes). The obtained values are given in Table 3. One may observe from this table that no value of the transition collapsed level is available for Test #7 since the latter started from an initial level of 2 m, *i.e.* well below the transition value of approximately 4 m, expected for a 300 kW power according to Tests #5 and #6.

Table 3: The estimated transition collapsed levels level from which the computed bubble fluxes exceeded 50% of the overall vaporization flux.

Test index	#1	#2	#3	#4	#5	#6	#7	#8	#9
Heating power (kW)	93	93	93	93	300	300	300	220	50
Loading pattern ref.	LP1	LP2	LP3	LP4	LP2	LP3	LP2	LP3	LP3
Transition collapsed level (m)	3.0	2.9	2.5	2.8	4.2	3.9	X	3.5	1.9

Next, regarding the boundary between the flashing and boiling modes, we considered as a best-estimate the experimental collapsed level value of 2.25 m, common for all tests, from which the bubbles produced by boiling within the heated bundles were able to reach the free surface (this value is reported in [15]). One may observe that, in link with the weak effect of the loading pattern on the time-trend of the bubble mass flux already discussed in Section 4.2, the MIDI facility vaporization regimes maps is, in the limits of the tested parameters, insensitive to variations in the heat source spatial distribution.

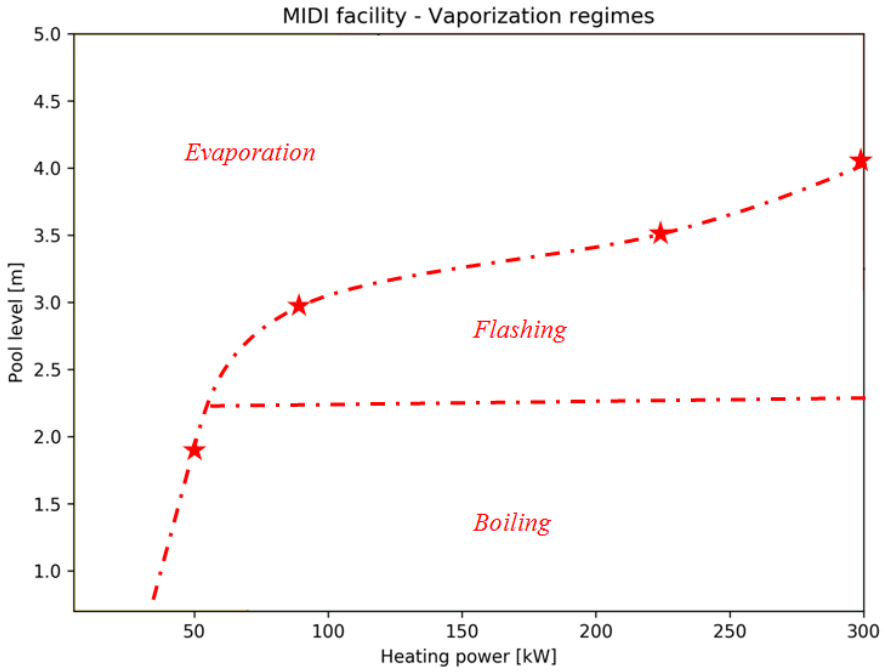

Figure 14: The MIDI facility vaporization regimes map. In red are represented the actual limits of those domains, estimated on the basis of the MIDI test results analysis.

5. A CHARACTERIZATION OF THE SINGLE-PHASE REGIME

In this section are developed two correlations quantifying the intensity of the single-phase natural convection heat and mass transfers. As already discussed in the introduction of the present paper, a natural convection flow is expected to develop at pool-scale in the studied accidental scenario. This flow

is the key mechanism of the transfer of heat from the bottom hot source to the colder pool free surface, but also of dissolved gases, from the supersaturated liquid bulk towards any available gas/liquid interface as illustrated in Figure 15. Three dimensionless numbers are classical descriptors of those heat and mass transfers. The first is the liquid-side *Rayleigh* number, denoted as Ra_L and equal to:

$$Ra_L = \frac{g\,\beta_L\,(T_h - T_i)\,d^3}{\vartheta_L\,\kappa_L}$$

with g the gravitational acceleration, β_L the liquid thermal expansion coefficient, T_h and T_i, respectively the heat source and free surface temperatures, d a length variable characterizing the treated problem and ϑ_L and κ_L, respectively the liquid kinematic viscosity and thermal diffusivity. This number characterizes the natural convection flow which triggers the studied heat and mass transfers (*i.e.* it represents the *ratio* between the buoyancy and dissipative forces (viscosity, conduction) triggering that flow). The next important quantity is the so-called *Nusselt* number Nu_L, which is a dimensionless form of the liquid-side heat transfer coefficient, here denoted as k_L. This number reads:

$$Nu_L = \frac{k_L\,d}{\lambda_L}$$

with λ_L the liquid thermal conductivity. Similarly for the mass transfer coefficient, denoted as $k_L^{O_2}$ for the dissolved oxygen species, measured within the MIDI basin (*cf.* [15]), one can introduce a so-called *Sherwood* number $Sh_L^{O_2}$ expressed as:

$$Sh_L^{O_2} = \frac{k_L^{O_2}\,d}{D_{w-O_2}}$$

with D_{w-O_2}, the dissolved oxygen diffusion coefficient in water. In what follows, those three numbers are combined in order to correlate the single-phase data of all achieved MIDI tests.

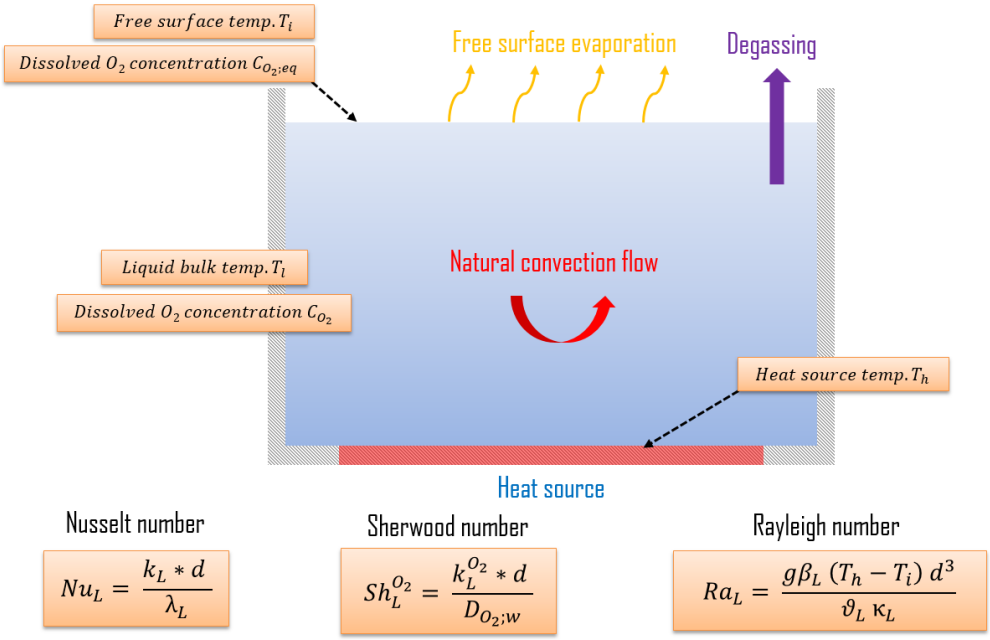

Figure 15: An idealization of the heat and mass transfers taking place within the MIDI basin during an experimental single-phase regime.

5.1. The natural convection heat transfer

A specific type of power law involving the so-called *Nusselt* Nu_L and *Rayleigh* Ra_L dimensionless numbers is commonly used in natural convection heat transfer [24]. This law reads:

$$Nu_L = C\, {Ra_L}^n$$

with C and n, the so-called prefactor and exponent of the law, that are classically adjusted against some relevant experimental data. This type of law, which is an obvious candidate for correlating the MIDI data, was tested against the single-phase stage of all achieved experiments. There are actually many ways of defining the above *Nusselt* and *Rayleigh* numbers on the basis of the available results, depending on which boundary temperatures and characteristic length d are retained. However, only one combination has proven able to reproduce the data with a significant trend and a limited dispersion. This combination reads:

$$\begin{cases} Nu_L = \dfrac{j_w\, L_v\, d}{(T_h - T_i)\lambda_L} \\ Ra_L = \dfrac{g\, \beta_L\, (T_h - T_i)\, d^3}{\vartheta_L\, \kappa_L} \end{cases}$$

with $j_w\, L_v\, /\, (T_h - T_i)$, an estimate of the single phase heat transfer coefficient k_L, j_w the overall vapor flux introduced in Section 4.1, L_v the water latent heat estimated at the free surface temperature T_i, d

the pool collapsed level given in [15] and T_h an enthalpy-flux-averaged hot source temperature, defined as:

$$T_h = \frac{\dot{m}_{hot}}{\dot{m}_{hot} + \dot{m}_{cold}} T_{hot} + \frac{\dot{m}_{cold}}{\dot{m}_{hot} + \dot{m}_{cold}} T_{cold}$$

and with $\dot{m}_{hot}$ and $\dot{m}_{cold}$, the cold and hot heated bundles overall mass flow rates, and T_{hot} and T_{cold}, the hot and cold heated bundles outlet liquid temperatures, as depicted in Figure 16.

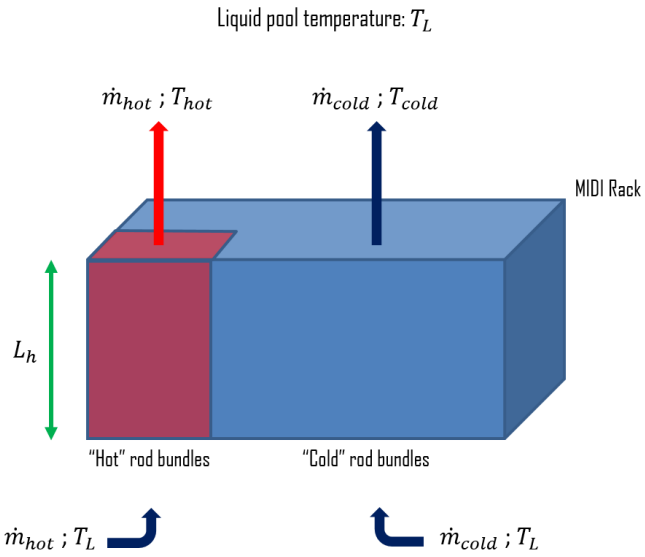

Figure 16: Illustration of the variables involved in the computation of the enthalpy-flux-averaged hot source temperature T_h.

The obtained results are plotted in Figure 17. First of all, the *Nusselt* and *Rayleigh* numbers of all the achieved tests appear significantly correlated through the form of the power law suggested above, with an average regression coefficient of 0.70. The law obtained for the single phase regime of those tests is thus equal to:

$$Nu_L = 0.11\ {Ra_L}^{0.33}$$

where one can recognize the typical value of 0.33 of the law's exponent, relating to natural convection turbulent flows and a prefactor of 0.11, which is of the order of magnitude of its expected values [24]. Significantly, this law is fairly close to the one that has been determined by means of fluid dynamics *direct numerical simulations* conducted by *Hay* in [25]:

$$(Nu_L)_{DNS} = 0.18\ {Ra_L}^{0.30}$$

which gives more confidence in the obtained results. Most of all, the heat source loading pattern seems to play a negligible role in the single phase heat transfer developing at pool scale, since all the presented tests follow a similar trend, with little variations. Noticing that the exponent of the obtained correlation

is of 0.33, the law is hence length-invariant (indeed, the length variable d in the *Nusselt* number cancels out with the term d^3 of the *Rayleigh* number, which is raised to the power of 0.33). In addition, both the present and *Hay*'s correlations can be compared with the data acquired by means of the Aquarius experimental device, detailed in [16]. As for the estimate of the *Nusselt* and *Rayleigh* numbers of the MIDI tests, the pool collapsed level is retained as the length variable d for processing the Aquarius data. Figure 17 shows the obtained results. As one can observe, the single-phase regime power law found from MIDI experiments complies with the Aquarius data. At last, this result allows extending the validity interval in terms of *Rayleigh* numbers of this power law towards smaller values. The law can be hence considered valid for $10^{10} < Ra_L < 10^{14}$.

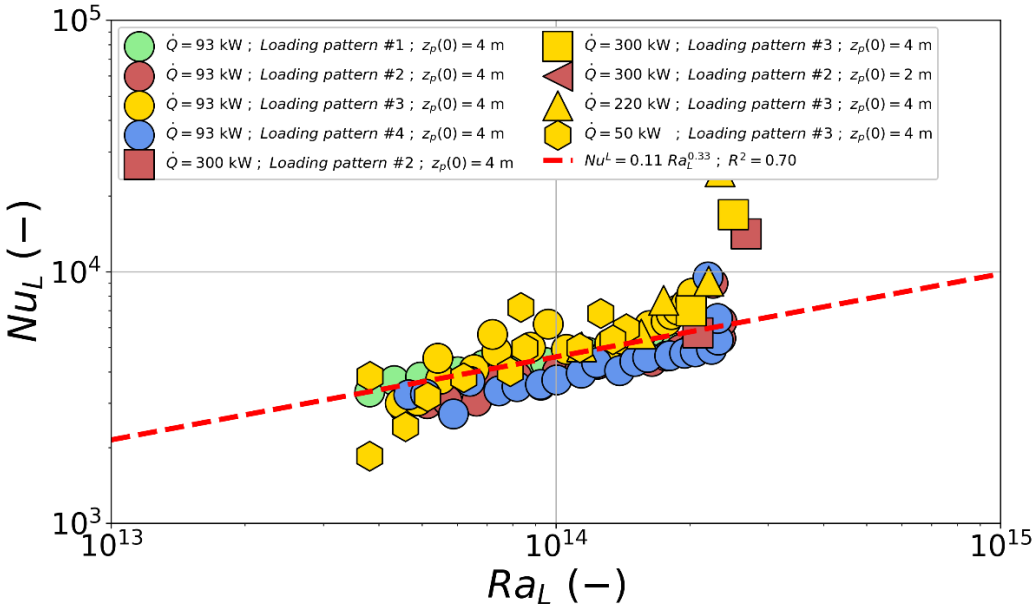

Figure 17: The *Nusselt* versus *Rayleigh* numbers natural convection heat transfer correlation obtained in the single-phase regime. For clearliness, only one data point out of twenty is plotted for every test.

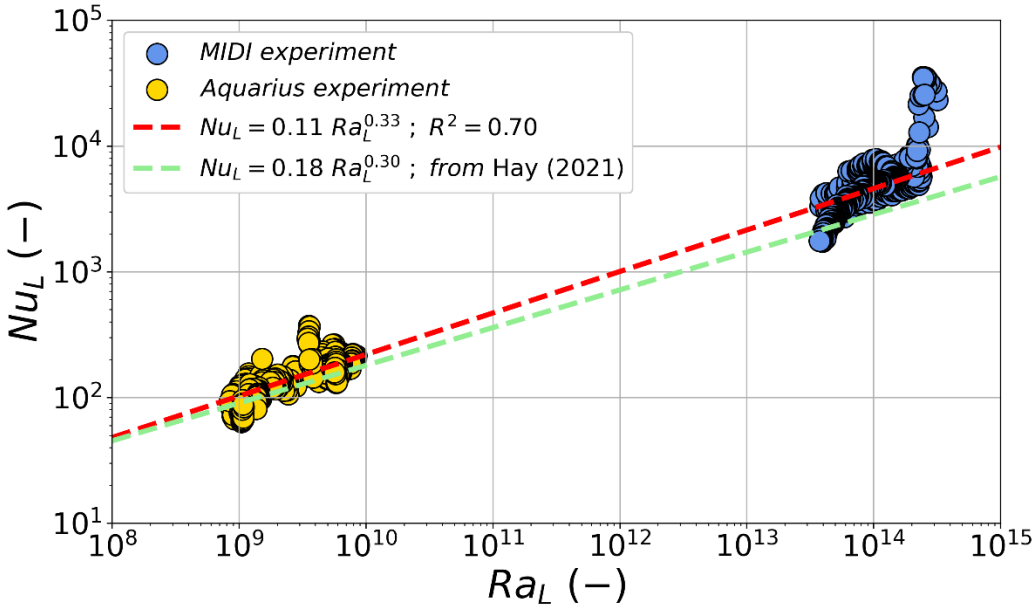

Figure 18: The *Nusselt* versus *Rayleigh* numbers in the single-phase regime obtained on the basis of MIDI and Aquarius data. Both datasets comply with the *Nusselt* versus *Rayleigh* power law determined from MIDI data.

5.2. The single-phase dissolved oxygen degassing

In the single-phase stage of any MIDI test, the liquid, initially saturated with dissolved gases, gradually degasses through any available gas/liquid interface, as discussed in Section 3.2. The whole part of this stage is characterized by a lack of bubble nucleation, the latter phenomenon occurring moderately, only when liquid temperatures get close to thermal saturation. Hence in this configuration, most of the dissolved gases mass transfer taking place in between the supersaturated liquid bulk and the available gas/liquid interfaces is to be dominated by the single-phase natural convection flows developing at pool scale. The latter flows being well described by means of the *Rayleigh* number Ra_L, as shown beforehand, one may thus expect an analogous relationship between Ra_L and the *Sherwood* number Sh_L associated with the degassing process, through the form:

$$Sh_L = C\ \ {Ra_L}^n$$

Such a relation was tested against the single-phase regime data of all MIDI tests and applied to the only monitored dissolved gases species composing the air: the O_2. For that purpose, its corresponding *Sherwood* number, denoted as $Sh_L^{O_2}$, was evaluated as follows:

$$Sh_L^{O_2} = \frac{j_{O_2}\ d}{\left(C_{O_2} - C_{O_2;eq}\right) D_{w-O_2}}$$

with j_{O_2}, the dissolved oxygen degassing flux post-processed from the data given in [15], d the same length variable as for the heat transfer correlation (see Section 5.1), D_{w-O_2}, the dissolved oxygen diffusion coefficient in water and C_{O_2}; $C_{O_2;eq}$, respectively the measured dissolved oxygen concentration reported in [15] and $C_{O_2;eq}$ its expected equilibrium value at the liquid bulk temperature which varies during the transient according to the so-called *Henry's law*. In a similar fashion than for the heat transfer, a correlation of the above proposed type complies too with the oxygen degassing data, as seen in the below Figure 19. This correlation reads:

$$Sh_L^{O_2} = 4.48\ {Ra_L}^{0.33}$$

It is not surprising to come up with a power law exponent of 0.33 similar to the one determined in Section 5.1, since the same single-phase turbulent natural convection flows are expected to trigger both heat and mass transfers at pool-scale. One can see that the correlation gets less predictive for larger values of the Ra_L numbers (*cf.* right-hand-side of the graph in Figure 19). We can here postulate the effect of the dissolved gases bubbles which are to nucleate when the liquid temperatures get close to saturation. At last, this correlation does appear almost independent from the loading pattern of the heat source, as noticeable in Figure 19.

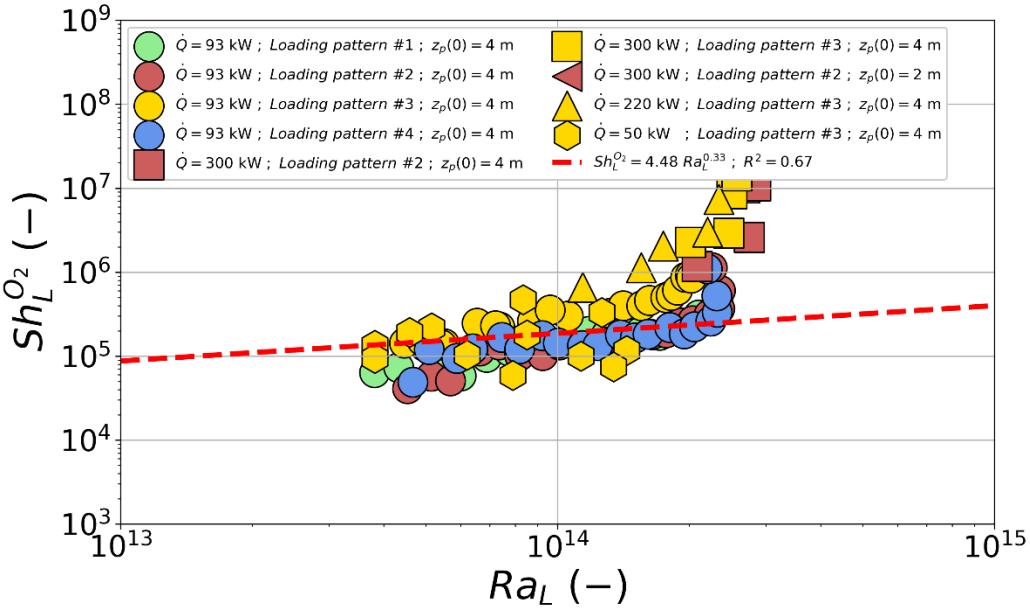

Figure 19: The *Sherwood* versus *Rayleigh* dissolved oxygen degassing correlation obtained in the single-phase regime. For clearliness, only one data point out of twenty is plotted for every test.

6. A CHARACTERIZATION OF THE TWO-PHASE REGIME

In the two-phase regime, the bubbles produced by gravity-driven flashing and/or boiling are expected to enhance the natural convection heat transfer developed at pool scale [26], [27] and the *Nusselt* number of any heat exchange within the liquid bulk is expected to deviate from its single-phase value. Though

there exists no consensus about a universal form of a *Nusselt* model for describing those two-phase heat transfers, the enhancement effect provided by the bubbles is often taken into account through the form of a bubble *Froude* number, which reads [28]:

$$Fr_b = \left(\frac{j_b}{\rho_g}\right)^2 \frac{1}{g\ d}$$

where j_b is the bubble mass flux as computed in Section 4.1, ρ_g is the gas density of the considered bubbles, g is the gravitational acceleration and d a vertical characteristic length, here naturally equal to the pool collapsed level. Furthermore, when there exists a conjugate heat and mass transfer between the liquid bulk and the bubbles (*e.g.* when the liquid vaporizes onto the bubbles), a so-called *Jakob* number is often useful when attempting to correlate the data of a two-phase heat transfer. This number reads:

$$Ja = \frac{Cp_l\ \Delta T_{eq}}{L_v}$$

with Cp_l the isobaric heat capacity of the liquid, ΔT_{eq} the temperature difference leading to the liquid vaporization (or condensation) with regards to the bubble and L_v, the latent heat. On that basis, many combinations of those two additional numbers and the classical Nusselt and Rayleigh numbers have been tried and only two of them have proven able to reproduce the MIDI two-phase data. The obtained correlations are detailed below. In the present case, it is interesting to identify a *Nusselt* correlation for each of the two modes of vaporization observed during the MIDI experiments, *i.e.* the bubbly vaporization (gravity-driven flashing and/or boiling) and the free surface evaporation. For that purpose, two *Nusselt* numbers, respectively denoted as Nu_b and Nu_e are defined:

$$\begin{cases} Nu_b = \dfrac{j_b\ L_v\ d}{(T_h - T_{sat})\lambda_L} \\ Nu_e = \dfrac{j_e\ L_v\ d}{(T_h - T_i)\lambda_L} \end{cases}$$

with j_b and j_e, respectively the bubble and evaporation mass fluxes, as computed in Section 4.1, d, the pool free surface diagonal. Identically, two vaporization-mode-related Jakob numbers are introduced:

$$\begin{cases} Ja_b = \dfrac{Cp_l(T_h - T_{sat})}{L_v} \\ Ja_e = \dfrac{Cp_l(T_h - T_i)}{L_v} \end{cases}$$

In doing so, we implicitly assume that the heat transfer which leads to the liquid vaporization onto the bubbles is achieved in between the hot liquid rising from the heated bundles, at the temperature T_h and the bubbles, mainly made of vapor, at the temperature $T_{sat} \approx T_{sat}(P_g)$. Similarly, it is assumed that the free surface evaporation is triggered by the heat transfer between some hot liquid at temperature T_h and the free surface at temperature T_i. Two correlations have been identified between those many numbers. They read:

$$\begin{cases} Nu_b = 4.38 \times 10^5 \times {Fr_b}^{0.39} {Ja_b}^{-0.45} \\ Nu_e = 3.04 \times 10^{-1} \times {Fr_b}^{0.42} {Ja_e}^{-4.67} \end{cases}$$

with a respective R^2 regression coefficient of 0.91 and 0.98. The data correlated that way is also plotted in Figures 20 and 21. Many points are to be discussed. First of all, the obtained correlations do appear insensitive to the loading pattern of the heat source, in consistency with what has been seen in Section 4.2. Next, for both correlations, a high bubble *Froude* number, reflecting a high bubble mass flux, leads as expected to an enhancement of the *Nusselt* number. Interestingly, the *Jakob* number does play the opposite role. The magnitude of the *Jakob* number reflecting the thermodynamic disequilibrium between the liquid bulk and the considered gaseous interface, high values of that number are expected to yield strong vaporization mass fluxes, and *vice versa*. Having this in mind, one can postulate that the vaporization process disturbs the liquid-side thermal boundary layer that is to develop at the location of the gas-liquid interface, thereby explaining this opposite effect of the *Jakob* number on the *Nusselt* one. One may wonder the likelihood of this assumption. At least one recent DNS study reproducing the bubbling in a pool mentions this effect [27]. Thus, the hypothesis seems to deserve more attention in order to consolidate the above proposed model of a two-phase heat transfer in a pool heated from below.

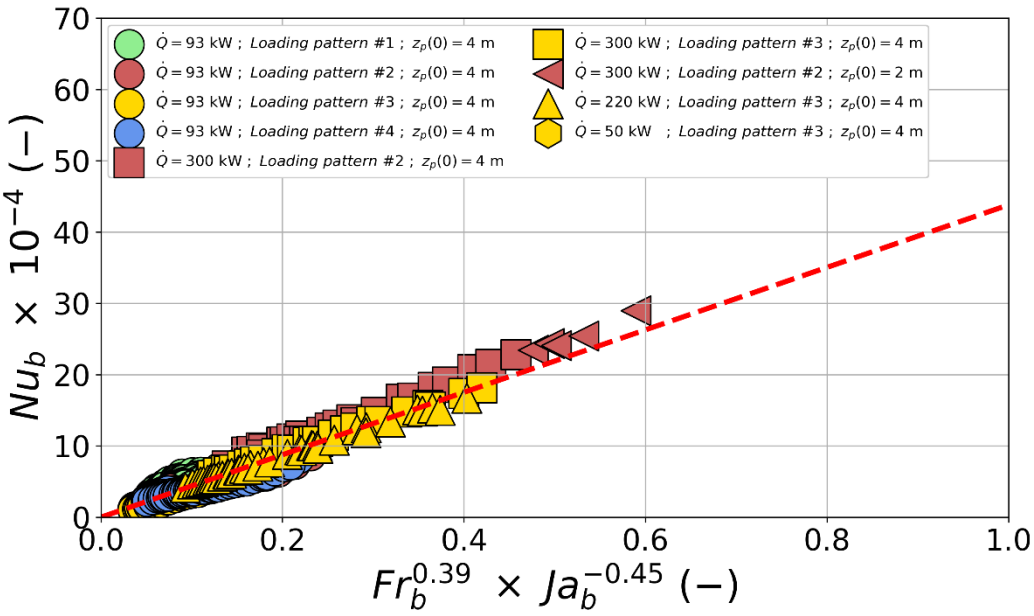

Figure 20: The liquid-to-bubble heat transfer correlation obtained in the two-phase regime. For clearliness, only one data point out of twenty is plotted for every test.

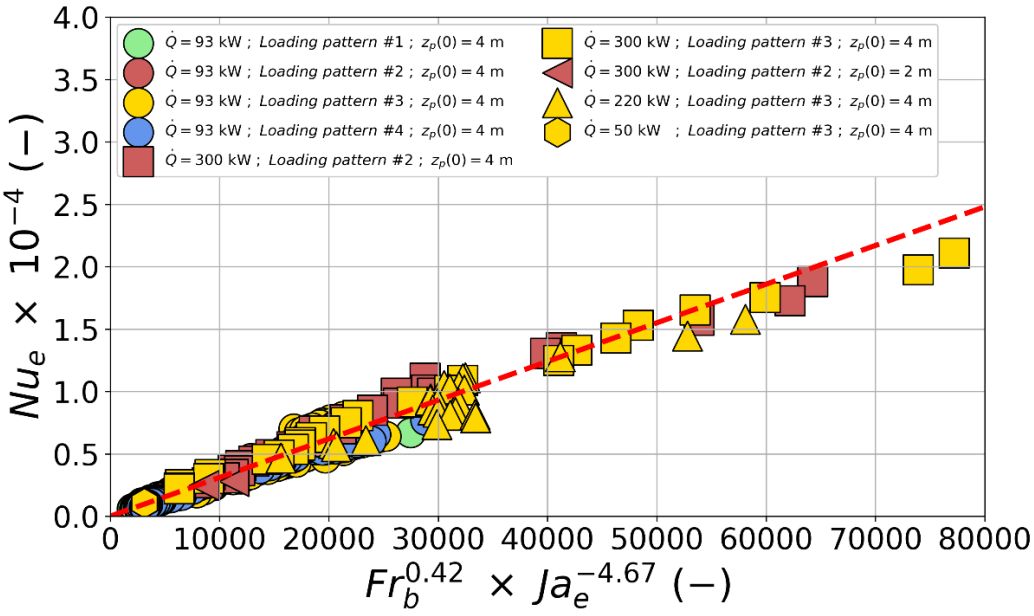

Figure 21: The liquid-to-free-surface heat transfer correlation obtained in the two-phase regime. For clearliness, only one data point out of twenty is plotted for every test.

7. CONCLUSIONS AND PERSPECTIVES

In this article, a first interpretation of the MIDI test results available to date has been proposed. The analysis has first focused on the phenomenological features of the test data. It has been shown that the actual overall phenomenology mostly complies with the one that was envisioned by the community right after the Fukushima-Daiichi nuclear accident. Indeed, the existence of a gravity-driven flashing of superheated water in a pool heated from below, a hypothetical phenomenon at that time, has been evidenced. Those results, obtained within the MIDI facility, are in complete agreement with the ones of an analytical test device of smaller scale operated at IRSN, referred to as Aquarius. The modes of flashing occurrence in this very configuration have been clarified too. Contrarily to the prior expectation that the phenomenon would preferentially occur onto any unheated immersed surfaces such as the lateral walls of the basin, the latter actually develops within the liquid bulk, as during the Aquarius experiments. Next, it has been emphasized that the degassing process is mostly completed before the liquid flashes/boils-off and maintains for some short while. In the MIDI facility, the dissolved gases are hence likely to play some role in the occurrence of flashing when the liquid starts superheating. However, yet at MIDI scale, the flashing phenomenon typically lasts a long time after the liquid is completely degassed, which questions the origin of the gaseous *nuclei* after the complete depletion in dissolved gaseous species. Regarding this observation, it can be postulated that, even if the degassing process is complete during the long-lasting flashing period, some new gas *nuclei* might be produced by air entrapment from the liquid free surface, when bubbles burst through the latter. Then, the role of the heat source pattern on the void fraction field has been highlighted, with however no evidence of any two-phase flow instability within the simulated spent fuel bundles.

Later, an analytical modeling of the vapor diffusion process taking place on top of the liquid free surface has been proposed. On the basis of the available MIDI experimental data, this modeling has allowed determining the fraction of the overall vapor flux which can be attributed to the free surface evaporation and the one due to the bubbles bursting at that very location. By applying the model, those fluxes have been quantified for each achieved MIDI test. Contrarily to the phenomenological observation of an effect of the loading pattern on the void fraction distribution, the latter heat source configuration has merely no impact on the value taken by those fluxes. In addition, a so-called vaporization regimes map, which predicts the dominant vaporization mode against the pool level and total heat power, has been reconstructed from the experimental data.

At last, the obtained data has been reduced through the form of a set of dimensionless correlations, involving some of the classical numbers in the field of heat and mass transfers. The free surface evaporation, degassing of dissolved non-condensable species and bubbles release processes have been all modeled by means of a simple mathematical formulation. Then, those models have been cross-compared, when relevant, with the Aquarius experimental results and with the output of some fluid dynamics direct numerical simulations. Significantly, the defined single-phase heat transfer correlation is fairly close to the one that has been determined by means of the two latter ways, which gives more confidence in the obtained results.

As an overall perspective, it appears worth going beyond those promising results and further characterize the impact of the heat source loading pattern on the void fraction distribution within the pool basin. The origin of the gaseous *nuclei* leading to the onset of flashing needs to be investigated too, either at the

smaller scale of the Aquarius device or numerically. Finally, according to the need of developing finer thermal-hydraulic simulation tools for treating the studied accidents, such as computational fluid dynamics codes, it could be beneficial to get finer data, in space and time, related to the phasic velocities, temperatures and void fraction, within the MIDI basin. This is an important outlook of the present work.

8. ACKNOWLEDGMENTS

The DENOPI project was part of the "Investment for the future" program funded by the French Government within the framework of the post-Fukushima surveys identified as major safety issues (contract number ANR 11 - RSNR 006). The French Government and the National Research Agency are gratefully acknowledged for their interest and financial support. Besides, IRSN thanks its project partners, US-NRC, Bel-V and EDF, for their valuable contributions.

9. REFERENCES

[1] EPRI (2012). “Summary of the EPRI Early Event Analysis of the Fukushima Daiichi Spent Fuel Pools Following the March 11, 2011 Earthquake and Tsunami in Japan – 2012 Technical Update”, Technical Report No. 1025058

[2] OECD/NEA (2014). “Status Report on Spent Fuel Pools under Loss-of-Cooling and Loss-of-Coolant Accident Conditions – Final Report”, Technical Report NEA/CSNI/R(2015)/2

[3] OECD/NEA (2018). “Phenomena Identification and Ranking Table: R&D Priorities for Loss-of-Cooling and Loss-of-Coolant Accidents in Spent Nuclear Fuel Pools”, Technical Report NEA/CSNI/R(2017)/18

[4] J.-M. Delhaye, M. Giot and L. Riethmuller (1981). “Thermohydraulics of two-phase systems for industrial design and nuclear engineering”, McGraw-Hill Book Company

[5] X. Lu and A. Watson (2002). “A review of geysering flows”, in Proc. 24th NZ Geothermal Workshop

[6] D. W. Murphy (1965). “An experimental investigation of geysering in vertical tubes”, Advances in Cryogenic Technology I-7, pp. 353-359

[7] Y. Liao and D. Lucas (2017). “Computational modeling of flash boiling flows: A literature survey”, International Journal of Heat and Mass Transfer, Vol. 111, p. 246

[8] F. Yan and M. Giot (1989). “Mechanisms of nucleation in flashing flows”, in Proc. 7th EUROTHERM Seminar, Thermal Non-Equilibrium in Two-Phase Flow, Roma, Italy, March 23-24, 1989

[9] J. Huyghe, G. Barois, A. Michel and H. Mondin (1968). “Etude expérimentale de l’autovaporisation en eau stagnante faiblement surchauffée et analyse de l’écoulement en canal d’un liquide en cours de détente”, Desalination, Vol. 4, pp. 209-219

[10] A. Bousbia-Salah and J. Vlassenbroeck (2012). “Survey of some safety issues related to some specific phenomena under natural circulation flow conditions”, in Proc. EUROSAFE 2012, November 5-6, 2012, Brussels, Belgium

[11] R. B. Duffey, U. Rohatgi and E. D. Hughes. (1993). “Two-phase flow instability and dryout in parallel channels in natural circulation”, in Proc. National Conference and Exposition on Heat Transfer, August 8-11, 1993, Atlanta, Georgia, USA

[12] J. Martin, G. Brillant, C. Duriez, N. Trégourès and C. Marquié (2017). "The IRSN DENOPI project: a research program on spent-fuel-pool loss-of-cooling and loss-of-coolant accidents", in Proc. 17th NURETH conference, Xi'an, China, September 3-8, 2017

[13] B. Migot, G. Brillant, J. Martin and S. Morin (2022). "DENOPI project devoted to spent fuel pool accidents: overview of the thermal-hydraulics experimental facilities", in Proc. 19th NURETH conference, Brussels, Belgium, March 6-11, 2022

[14] J. Martin and N. Trégourès (2023). "OECD/NEA R&D priorities for loss-of-cooling and loss-of-coolant accidents in Spent-Fuel-Pools", Nuclear Engineering and Design, Vol. 410, pp. 112380

[15] B. Migot and J. Martin (2024). "An experimental study of the thermal-hydraulics of a spent nuclear fuel pool under loss-of-cooling accident conditions. Part I: the MIDI facility and its main experimental results", Nuclear Engineering and Design, *on press*

[16] J. Martin (2023). "The gravity-driven flashing of metastable water in a pool heated from below – An experimental study", PhD thesis, Université Catholique de Louvain, Institute of Mechanics, Materials and Civil Engineering, Louvain-la-Neuve, Belgium

[17] J. Martin, P. Ruyer, M. Duponcheel and Y. Bartosiewicz (2023). "A novel experimental observation of the gravity-driven flashing of metastable water in a heated pool", Nuclear Engineering and Design, Vol. 410, pp. 112371

[18] Y. Liao and D. Lucas (2017). "Computational modeling of flash boiling flows: A literature survey", International Journal of Heat and Mass Transfer, Vol. 111, pp. 246

[19] R. Bird, W. Stewart and E. Lightfoot (2007). "Transport Phenomena – Revised Second Edition", John Wiley & Sons

[20] J. Martin and B. Migot (2019). "Experimental study of the surface evaporation rate of a heated water pool at high temperature using infrared thermography", in Proc. 18th NURETH conference, Portland, Oregon, USA, August 18-22, 2019

[21] J. H. Lienhard IV and, J. H. Lienhard V (2008). "A heat transfer textbook", Third edition, Phlogiston press, Cambridge, Massachusetts

[22] S. Bower and J. Saylor (2009). "A study of the Sherwood-Rayleigh relation for water undergoing natural convection-driven evaporation", International Journal of Heat and Mass Transfer, Vol. 52, pp. 3055

[23] J. Martin, T. Kamin and P. Ruyer (2017). "Analysis of the Fukushima-Daiichi Unit-4 Spent Fuel Pool loss-of-cooling accident by means of the TETHYS code: highlight of major thermal-hydraulic modeling issues", in Proc. 17th NURETH conference, Xi'an, China, September 3-8, 2017

[24] J. S. Turner (1973). "Buoyancy effects in fluids", Cambridge University Press

[25] W. Hay (2021). "Evaporation-driven turbulent convection in water pools heated from below", PhD thesis, Université Catholique de Louvain, Institute of Mechanics, Materials and Civil Engineering, Louvain-la-Neuve, Belgium

[26] F. G. Blottner (1979). "Hydrodynamics and heat transfer characteristics of liquid pools with bubble agitation", NUREG/CR-0944, SAND79-1132 R3

[27] R. Lakkaraju, R. Stevens, P. Oresta, R.Verzicco, D. Lohse and A. Prosperetti (2013). "Heat transport in bubbling turbulent convection", PNAS, Vol. 110, pp. 9237-9242

[28] M. Amizic, E. Guyez and J. M. Seiler (2012). “Experimental investigation on heat transfer for two-phase flow under natural convection”, in Proc. ICONE20-POWER2012-55225, pp. 767-773